

1 Feb 23, 2008
2
3

4 **APPENDIX I. THE NATURE OF He DIFFUSION IN THE MANTLE**

5 He diffusion parameters have been published for olivine, clinopyroxene, garnet and
6 basalt melt. The relevant diffusion parameters and Arrhenius curves for the various phases are
7 shown in Figure A1. Two measurements of He in olivine have been reported (Hart, 1984; Trull
8 and Kurz, 1993), and are in good agreement. Both are slower than He diffusion in cpx and
9 garnet, at temperatures below 1500°C (Trull and Kurz, 1993; Dunai and Roselieb, 1996; Aciego
10 et al. 2003; Roselieb et al., 2006), and several orders of magnitude slower than He in basalt melt
11 (Kurz and Jenkins, 1981; Trull, 1989; Trull and Kurz, 1999). The garnet measurements of
12 Aciego et al. (2003) are quite different from those of Dunai and Roselieb (1996) and Roselieb et
13 al. (2006), reflecting the different garnet compositions and different techniques used. Aciego et
14 al. measured the release of natural He from a grossular-almandine-rich garnet during annealing
15 in vacuo at 800°C - 1300°C. Dunai and Roselieb measured the sorption rate of He into
16 almandine-rich pyropes, during annealing at 800°C - 990°C at 250 bars. The same garnet was
17 studied by Roselieb et al. at 7 kbar, with results that agreed within stated uncertainties. In all of
18 these cases, the garnets were metastable under the annealing conditions utilized, so that incipient
19 decomposition could be a factor in the measured diffusion parameters.

20 We have not considered the ${}^3\text{He}$ diffusion coefficients measured for cosmogenic ${}^3\text{He}$ in
21 olivine (Trull et al., 1991) or the measurements on olivine using proton-induced ${}^3\text{He}$ (Shuster et
22 al., 2003). Both give similar results, with rather low activation energies, and in the temperature
23 range measured (280° – 640°C) show diffusion coefficients many orders of magnitude higher
24 than the olivine results in Figure A1 (extrapolated to similar temperatures). We believe these
25 results are compromised by radiation damage effects (see discussion in Trull et al., 1991), and in

any event require very large upward extrapolations in temperature to be relevant to the modeling here. Ironically, the extrapolated diffusion coefficients at 1500°-1700°C are $\sim 10^{-6}$ cm²/s, the same as used here for our modeling.

As might be expected, diffusion of ³He is slightly faster than diffusion of ⁴He ($9 \pm 4\%$ in olivine, Trull and Kurz, 1993; $12 \pm 2\%$ in basalt glass at 1100°C, Trull and Kurz, 1999); this difference can lead to fractionation of ³He and ⁴He; for example, for cases where diffusive losses of He from a reservoir are large (> 99%), ³He/⁴He can be lowered in the residue by >20%. A possible example of fractionations between olivine and clinopyroxene phenocrysts has been reported by Harrison et al (2004).

In general, grain-scale diffusive equilibrium is expected for most elements in most mineral assemblages in the mantle (Hofmann and Hart, 1978). This is particularly true for He, given it's relatively high diffusion rates. Large scale diffusion then will depend on the fastest mineral pathways, with grain-boundary processes possibly playing a significant role. The formulation for effective diffusion rates, as a combination of volume and grain-boundary (or other "short-circuit") processes (Lee, 1995), can be written (for small f) as:

$$D_{\text{effective}} = D_v + K * f * D_{\text{sc}} \quad (1)$$

where D_v is the volume diffusion coefficient, D_{sc} is the grain boundary or short-circuit diffusion coefficient, K is the partition coefficient of He between grain boundary and lattice sites, and f is the volume fraction of grain boundary or short-circuit paths in the total solid.

While there is one estimate of the partitioning of He between grain boundaries and diopside aggregates ($K \sim 10^4$ to 10^5 ; Baxter et al., 2007) that shows some potential for a bulk

49 transport pathway, there are no data on grain boundary He diffusion rates. On the other hand, for
50 the case of a lherzolite containing a partial melt network, data does exist for both K and D_{sc} , and
51 an estimate of $D_{effective}$ can be made. Literature values for K (He partition coefficient between
52 silicate melt and olivine) range from an upper limit of ~ 150 (Parman et al., 2005) to a lower
53 limit of ~ 5900 (Heber et al., 2007). For a 1% interconnected melt porosity, with helium
54 diffusion in an alkali basalt melt $\sim 100x$ diffusion in olivine (at $\sim 1550^{\circ}\text{C}$, fig. 1), $D_{effective}$ could
55 range from 150 D_v to 5900 D_v . While this is a very large increase in effective diffusion rates, it
56 will be offset by the fact that mantle domains spend relatively short periods of time above their
57 solidus (compared to potential deep mantle residence times of several Gy). For example, at a
58 upwelling rate of 20 mm/year, a mantle domain will traverse the melting zone in only 3 My.

59 For the purposes of this paper, we present conservative diffusive equilibration
60 calculations, using the diffusion rate of He in olivine. This will give lower limits for scale-
61 lengths of He equilibration between mafic layers and a peridotite matrix, as the faster rates
62 through cpx, garnet, grain boundaries, and melt networks will only serve to increase the scale-
63 lengths of equilibration. We do not consider here other processes that may enhance He re-
64 distribution, such as stirring and mixing, or advective transport of melt.

65 The extant diffusion data applies to mantle depths above the transition zone, as the
66 minerals discussed above are only stable above 410 km. The effect of pressure on He diffusion in
67 upper mantle minerals is essentially unknown; typically, increasing pressure will lead to slower
68 diffusion, but this effect is also mitigated by the increase of temperature along an upper mantle
69 adiabat. The garnet results of Roselieb et al. (2006) at 7 kb did not show a significant pressure
70 effect compared to the 250 bar data of Dunai and Roselieb (1996); see Fig. A1.

71 In the modeling below, we bracket the diffusion coefficients used between the best
72 estimate for the upper mantle potential temperature derived from MORB petrology, and the
73 projected temperature at 410 km based on a depleted upper mantle adiabat from the
74 thermodynamic model of Stixrude and Lithgow-Bertelloni (2005a,b). Petrologic estimates of
75 upper mantle potential temperatures under ridges are in the range $1350^{\circ}\text{C} \pm 50^{\circ}\text{C}$ (Courtier et al.,
76 2007); these are in agreement with estimates for global upper mantle of 1380°C (derived from
77 the average global width of the transition zone, Lawrence and Shearer, 2006, and the
78 thermodynamic model of Stixrude and Lithgow-Bertelloni, 2005a,b), and the northern Pacific
79 upper mantle, 1370°C (Schmerr and Garnero, 2006; Stixrude and Lithgow-Bertelloni, 2005a,b).
80 Petrologic estimates of hotspot mantle potential temperatures, derived from OIB data, average
81 1500°C (Courtier et al., 2007). These are similar to potential temperature estimates derived from
82 transition zone thickness data for Pacific mantle (centered on $10^{\circ}\text{N} - 150^{\circ}\text{W}$; Schmerr and
83 Garnero, 2006) of 1470°C . Projected along a thermodynamic upper mantle adiabat (Stixrude and
84 Lithgow-Bertelloni, 2005a,b), potential temperatures of 1350°C and 1500°C increase to 1540°C
85 and 1705°C respectively at 410 km. We will use this latter temperature range as an upper limit.

86 No diffusion data exists for He in deep mantle phases such as perovskite or
87 ferropericlase; it is not at all obvious that these phases will be “slow”. The temperatures in the
88 deep mantle will be much higher than those above 410 km, and there is also evidence from data
89 on elements such as Mg that both volume and grain boundary diffusion rates may be quite high
90 in deep mantle phases such as ferropericlase (Van Orman et al., 2003; Holzapfel et al., 2003).
91 Projecting an upper mantle potential temperature of 1500°C to the deepest mantle, using the
92 model of Stixrude and Lithgow-Bertelloni (2005a,b), leads to a CMB temperature of $\sim 2500^{\circ}\text{C}$.

93 As a purely illustrative exercise, extrapolation of the olivine data in Fig. A1 to this temperature
94 would generate a He diffusion coefficient some 2000 times larger than that at 400 km.

95

96 APPENDIX II. FOOTNOTES TO TABLE 1: U-Th-He INPUT PARAMETERS

97 Bulk Silicate Earth (BSE): See text. Note that if the Earth started at 4.53 Gy with a solar nebula
98 ${}^3\text{He}/{}^4\text{He}$ value of 120 Ra (Pepin and Porcelli, 2002), evolving to 50 Ra today, the required
99 ${}^{238}\text{U}/{}^3\text{He}$ value (today) would be 453, with ${}^3\text{He} = 4.13\text{E-}9 \text{ cc/g}$, ${}^4\text{He} = 5.94\text{E-}5 \text{ cc/g}$. These values
100 are only 34% different than those used in Table 1, and will not affect any of the modeling
101 conclusions.

102

103 Depleted MORB Mantle (DMM): See text. The U and Th values are taken from Workman and
104 Hart (2005). The derived ${}^3\text{He}$ concentration is very similar to the value of $1.68\text{E-}11 \text{ cc/g}$
105 estimated by Saal et al., 2002, based on their measurement of upper mantle CO₂ contents.
106 Starting with an initial ${}^3\text{He}/{}^4\text{He}$ value of 120 Ra (instead of 230 Ra) changes the ${}^{238}\text{U}/{}^3\text{He}$, ${}^3\text{He}$
107 and ${}^4\text{He}$ values for DMM today insignificantly relative to the values in Table 1 ($\sim 1.4\%$).

108

109 Ocean Crust (OC): Derivation of an ocean crust packet from DMM at 1.5 Gy could be modeled
110 with a simple melting model, assuming the ocean crust is a 6% melt of DMM (Workman and
111 Hart, 2005), and that helium is highly incompatible (Parman et al., 2005). This would lead to a
112 ${}^3\text{He}$ concentration of $\sim 3.93\text{E-}10 \text{ cc/g}$, and this is at the upper end of all MORBs. Measurements
113 that may be more realistic for mature ocean crust can be estimated from ocean crust gabbros and
114 peridotites, with ${}^3\text{He} \sim 1.0\text{E-}12 \text{ cc/g}$ (Atlantis Bank, Moreira et al., 2003; Kumagai et al., 2003).
115 These values are much lower, and would suggest a very high degree of crustal degassing during

116 solidification. In any event, it is likely that additional major helium degassing will occur during
117 ocean crust subduction (Moreira and Kurz, 2001); estimates for water and noble gas loss during
118 subduction lie in the 92-98% range (Staudacher and Allegre, 1988; Dixon et al., 2002). It will
119 turn out that the initial helium budget (after subduction) is inconsequential compared to the ^4He
120 production during 1.5 Gy of storage of ocean crust in the mantle.

121 Estimating U in ocean crust with the above simple melting model leads to a concentration
122 of 53 ppb. This is identical to the value derived by Hofmann (1988) for N-MORB, after
123 correcting back to a “parental” mantle melt. It is also similar to the 44 ppb U content of a 500 m
124 section of ocean crust gabbros from Site 735b (Hart et al., 1999). Upper oceanic crust of course
125 has substantially higher U contents, due to seawater alteration (Hart and Staudigel, 1989). For
126 our modeling, we have chosen a U content of 46 ppb, with Th/U = 2.5.

127 The real uncertainty arises, as with helium, with respect to what happens to U and Th
128 during the subduction processing of oceanic crust. From various mass balance considerations,
129 Kelley et al., (2005) estimate that <50% of U and none of the Th is lost to the arc and back-arc.
130 A similar conclusion is reached by looking at eclogites that may represent a “post-subduction”
131 version of ocean crust (Bebout, 2007). John et al (2004) showed that a large variety of eclogites
132 have U/Nb ratios similar to, or higher than MORB, suggesting little or no U loss during
133 subduction processing. Similarly, Becker et al (2000), in a suite of ~ 25 eclogites, found most of
134 them to have U and Th equal to or greater than fresh N-MORB, and none had unusually high
135 Th/U ratios. These findings are in agreement with experimental fluid/eclogite partitioning results
136 for U and Th, provided conditions do not involve removal of partial melt or supercritical fluid
137 (Kessel et al., 2005). We feel that our U and Th estimate for recycled oceanic crust is
138 conservative, and that a very high U+Th/ ^3He ratio for such ocean crust is inevitable. This of

139 course leads rapidly to substantial budgets of ^4He ($15 \mu\text{cc/g}$), and very low $^3\text{He}/^4\text{He}$ ratios (~ 0.05
140 Ra); recycled ocean crust is thus a formidable source of radiogenic ^4He !

141

142 APPENDIX III: RECYCLED OCEANIC CRUST SLAB IN AN AMBIENT BSE MATRIX

143 This case refers to ocean crust that is subducted into a BSE mantle 1.5 Gy ago, and
144 rapidly stretched and thinned to a 1 km thickness during convection. There is no evidence for the
145 survival of any BSE on earth (based on Sr, Nd, Pb and Hf isotopes), but this case is intended to
146 model a He-rich ambient mantle, to contrast with the He-depleted DMM mantle used above. ^3He ,
147 ^4He and $^3\text{He}/^4\text{He}$ profiles extending to 10 km on either side of the 1 km slab are shown in Fig.
148 A3. As in the case of a OC slab in DMM matrix, at all times ^3He diffusion is directed into the
149 slab, from the ambient BSE mantle (Fig. A3a). At present, this ocean crust slab is not fully
150 equilibrated for ^3He , consistent with curve D in Fig. 1. ^4He also starts low in the ocean crust and
151 increases rapidly due to production from U + Th (Fig. A3b); however, it never surpasses the high
152 ^4He content of the ambient BSE mantle, and ^4He is always directed into the slab. The present day
153 ^4He content of the slab is almost 3 times that of the “closed-system” value for the slab.

154 Fig. A3c shows the resulting $^3\text{He}/^4\text{He}$ profile for this case; due to the high He content of
155 the ambient BSE mantle, the $^3\text{He}/^4\text{He}$ of the slab very quickly approaches to within $\sim 6\%$ that of
156 the ambient mantle, and stays about 6% lower than BSE throughout the model time. As a result,
157 the He anomaly due to the slab is small and quite diffuse. In terms of its impact when sampled
158 over different sample volumes (Fig. A3d), it would likely be virtually unnoticeable, unless the
159 slab was thicker (see curve for 5 km slab, Fig. A3d).

160

161 **APPENDIX IV. MODEL CORRELATIONS AND MIXING BETWEEN He, Sr AND Nd.**

162 It is useful to compare the effects of domain sampling size on $^3\text{He}/^4\text{He}$, for the three 1
163 km-1.5 Gy models shown in Fig. 2, A3 and 3, with model profiles for Sr and Nd. Because
164 these latter elements have diffusion coefficients 3-7 orders of magnitude smaller than He
165 (Sneeringer et al., 1984; Van Orman et al., 1998, 2001; Cherniak, 2001), there will be virtually
166 no diffusion between the slab and ambient mantle. Diffusion could therefore lead to
167 “decoupling” between He and these elements. We illustrate this point by comparing the
168 relationship between $^{143}\text{Nd}/^{144}\text{Nd}$ and $^3\text{He}/^4\text{He}$ during sampling with different size domains – see
169 Fig. A4 (similar results were obtained for Sr, but these curves are not shown here). The He
170 concentration and isotopic data are taken from Table 1, and Sr and Nd concentrations and
171 isotopic data for the BSE, DMM and OC end-members are given in the caption to Figure A4.
172 Estimates are used where the He, Sr or Nd data is not well-constrained (the sense of the models
173 given in Fig. A4 will not change for any reasonable variants of this data).

174 For each of the three model cases, a simple “no diffusion” mixing curve is shown in each
175 panel of Fig. A4 as a dashed line. Depending on the Nd/He ratios of the end-members, these
176 mixing curves range from almost linear (OC slab in DMM) to markedly curved (OC slab in BSE;
177 BSE slab in DMM). The first observation is that the sampling curves including He diffusion are
178 virtually identical to the no diffusion mixing curves for sampling domains larger than ~ 10 km
179 (equivalent to slab components of less than $\sim 10\%$ in the simple mixing cases). The large
180 sampling volumes effectively “dilute” the slab component where the He diffusion effects are
181 prominent. The “with-diffusion” curves deviate more and more strongly as the sample domain
182 width decreases, and, particularly for the OC slab in BSE and the BSE slab in DMM, the
183 $^3\text{He}/^4\text{He}$ ratio becomes constant over a significant range of $^{143}\text{Nd}/^{144}\text{Nd}$.

184 There are natural situations where large variations in ${}^3\text{He}/{}^4\text{He}$ occur at constant values of
185 Sr or Nd. For example, on the islands of Ofu, Olosega and Ta'u, Samoa, ${}^3\text{He}/{}^4\text{He}$ varies from 15
186 Ra to 34 Ra (Jackson et al., 2007) at relatively constant values of ${}^{87}\text{Sr}/{}^{86}\text{Sr}$ ($\sim 0.70466 \pm 160$
187 ppm) and ${}^{143}\text{Nd}/{}^{144}\text{Nd}$ ($\sim 0.51281 \pm 25$ ppm). These can be understood in several ways. They
188 may represent sampling of large-domains containing small fractions of a He-rich slab, with or
189 without a diffusive component (as in the upper part of the curves in Fig. A4c). They may
190 represent sampling domains that do not actually “include” any slab (and thus do not see any Sr
191 and Nd from the slab), but only sample the “wings” of the He diffusion profiles exterior to the
192 slab (e.g. km-scale sampling of the ${}^3\text{He}/{}^4\text{He}$ profile of Fig. 3c between distances of 2-10 km from
193 the slab will supply melts with ${}^3\text{He}/{}^4\text{He}$ varying from 38 Ra to 8 Ra, at constant Sr and Nd
194 isotope ratios). This would be similar to the “ghost” helium of Albarede and Kaneoka (2007).

195 **APPENDIX V. ${}^3\text{He}/{}^4\text{He}$ EXCHANGE BETWEEN MIGRATING MELT AND LITHOSPHERE**

196 We briefly address here the issue of possible re-equilibration of He between migrating
197 melts and the mantle hosting the melt networks. In other words, does the He in an erupted melt
198 represent the mantle domain the melt was derived from, or has the melt diffusively “picked up”
199 the isotopic signature of shallower mantle along its transport path (for example, overlying
200 lithosphere)? We use the fractal melt network model of Hart (1993), with estimates of the
201 various controlling parameters as given in Table A1 (note that the He diffusion coefficient used
202 here is 10x smaller than that used in the slab modeling sections, due to the lower temperatures in
203 the uppermost mantle melting regimes). This is a qualitative calculation only, as several
204 parameters are not well constrained (e.g. the aspect ratio of the fractal conduits). Formally, it
205 appears that a melt will travel only distances of a few hundred meters before losing touch with
206 the mantle host. Little re-equilibration takes place after this transport length, partly because the

207 conduit size and melt velocity have become substantial, but also because of the very low
208 partition coefficient (taken here as 0.006; Parman et al., 2005) for He between olivine and melt
209 (a given parcel of melt needs to diffusively “mine” a large volume of peridotite before the He
210 isotopic concentration of the melt is perturbed). Of course, this does not mean that erupted melts
211 will ever preserve signatures of mantle domains on the hundred meter scale, as subsequent
212 mixing with melts from other downstream fractal “tributaries” will lead to much larger-scale
213 domain sampling.

214 One signature of melts that have partially re-equilibrated with overlying mantle would be
215 a case where variable $^3\text{He}/^4\text{He}$ is accompanied by constant Sr, Nd, Pb, etc. One such case is
216 discussed above (Appendix III). Another might be represented in the basalts from Loihi
217 seamount, where tholeiites show somewhat higher $^3\text{He}/^4\text{He}$ than alkali basalts, at fairly uniform
218 Sr, Nd and Pb ratios (Kurz et al., 1983). The alkali basalts may represent smaller degree, deeper
219 melts, thus exposed to a longer transport length, whereas the tholeiites may be both shallower,
220 larger degree melts, possibly traveling faster through the lithosphere.

221

Table A1

Parameters and Units	Value
d, grain size, cm	0.3
C, peridotite heat capacity, joules/g°K	1.25
R, mantle upwelling rate, cm/year	10
S, solidus slope, °C/km	3
a, adiabat slope, °C/km	0.4
L, enthalpy of fusion, joules/gram	775
D, He diffusion coefficient at 1500°C, cm ² /sec	1.0E-07
K, olivine/melt He partition coefficient	0.006
A, aspect ratio of fractal conduits, length/radius	2000
μ , viscosity, pascal-sec	1.5
$\Delta\rho$, melt/solid density contrast, g/cm ³	0.3

D is from Fig. 1; K is from Parman et al., 2005;
other values referenced in Hart, 1993.

222

223

224 **APPENDIX REFERENCES**

- 225 Aciego, S., Kennedy, B. M., DePaolo, D. J., Christensen, J. N., Hutcheon, I., 2003. U-Th/He age
226 of phenocrystic garnet from the 70 AD eruption of Mr. Vesuvius. *Earth and Planetary*
227 *Science Letters* 219, 209-219.
- 228 Albarède, F., Kaneoka, I., 2007. Ghost primordial He and Ne. *Geochimica et Cosmochimica*
229 *Acta* 71, A9.
- 230 Baxter, E. F., Asimow, P. D., Farley, K. A., 2007. Grain boundary partitioning of Ar and He.
231 *Geochimica et Cosmochimica Acta*, 71, 434-451.
- 232 Bebout, G. E., 2007, Metamorphic chemical geodynamics of subduction zones. *Earth Planetary*
233 *Science Letters*, 260, 373-393.
- 234 Becker, H., Jochum, K. P., Carlson, R. W., 2000, Trace element fractionation during dehydration
235 of eclogites from high-pressure terranes and the implications for element fluxes in
236 subduction zones. *Chemical Geology* 163, 65-99.
- 237 Cherniak, D. J., 2001. Pb diffusion in Cr diopside, augite, and enstatite, and consideration of the
238 dependence of cation diffusion in pyroxene on oxygen fugacity, *Chemical Geology* 177,
239 381-397.
- 240 Courtier, A. M., Jackson, M. G., Lawrence, J. F., Wang, Z., Lee, C-T. A., Halama, R., Warren, J.
241 M., Workman, R., Xu, W., Hirschmann, M., Larson, A. M., Hart, S. R., Lithgow-
242 Bertelloni, C., Stixrude, L., Chen, W-P., 2007. Correlation of seismic and petrologic
243 thermometers suggests deep thermal anomalies beneath hotspots, *Earth Planetary Science*
244 *Letters*, in press.
- 245 Dixon, J. E., Leist, L., Schilling, J. G., 2002. Recycled dehydrated lithosphere observed in
246 plume-influenced mid-ocean-ridge basalt. *Nature* 420, 385-389.
- 247 Dunai, T. J., Roselieb, K., 1996. Sorption and diffusion of helium in garnet: Implications for
248 volatile tracing and dating. *Earth and Planetary Science Letters* 139, 411-421.
- 249 Harrison, C., Barry, T., Turner, G., 2004. Possible diffusive fractionation of helium isotopes in
250 olivine and clinopyroxene phenocrysts, *European Journal of Mineralogy* 16, 213-220.
- 251 Hart, S. R., 1993. Equilibration during mantle melting: a fractal tree model, *Proceedings of the*
252 *National Academy of Science* 90, 11914-11918.
- 253 Hart, S. R., 1984. He diffusion in olivine. *Earth and Planetary Science Letters* 70, 297-302.
- 254 Hart, S. R., Zindler, A., 1986. In search of a bulk earth composition, *Chemical Geology*, 57, 247-
255 267.
- 256 Hart, S. R., Blusztajn, J. S., Dick, H. J. B., Meyer, P. S., Muehlenbachs, K., 1999. The
257 fingerprint of seawater circulation in a 500-meter section of ocean crust gabbro.
258 *Geochimica et Cosmochimica Acta* 63, 4059-4080.
- 259 Hart, S. R., Staudigel, H., 1989. Isotopic characterization and identification of recycled
260 components. in *Crust/Mantle Recycling at Convergence Zones*, Hart, S. R., Gülen, L.,
261 Eds. Kluwer Academic Publishers: Dordrecht, The Netherlands Vol. 258, Series C, pp
262 15-28.

- 263 Heber, V. S., Brooker, R. A., Kelley, S. P., Wood, B. J., 2007. Crystal-melt partitioning of noble
264 gases (helium, neon, argon, krypton and xenon) for olivine and clinopyroxene.
265 *Geochimica Cosmochimica Acta* 71, 1041-1061.
- 266 Hofmann, A., Hart, S. R., 1978, An assessment of local and regional isotopic equilibrium in the
267 mantle. *Earth and Planetary Science Letters* 38, 44-62.
- 268 Holzapfel, C., Rugie, D. C., Mackwell, S. J., Frost, D. J., 2003. Effect of pressure on Fe-Mg
269 interdiffusion in $(Fe_xMg_{1-x})O$ ferropericlase. *Physics of the Earth and Planetary Interiors*
270 139, 21-34.
- 271 Jackson, M. G., Kurz, M. D., Hart, S. R., Workman, R. K., 2007. New Samoan lavas from Ofu
272 Island reveal a hemispherically heterogeneous high $^3He/^4He$ mantle. *Earth and Planetary*
273 *Science Letters*, in press 2007.
- 274 John, T., Scherer, E. E., Haase, K., Schenk, V., 2004. Trace element fractionation during fluid-
275 induced eclogitization in a subducting slab: trace element and Lu-Hf-Sm-Nd isotope
276 systematics. *Earth and Planetary Science Letters* 227, 441-456.
- 277 Kelley, K. A., Plank, T., Farr, L., Ludden, J., Staudigel, H., 2005. Subduction cycling of U, Th,
278 and Pb. *Earth and Planetary Science Letters* 234, 369-383.
- 279 Kessel, R., Schmidt, M. W., Ulmer, P., Pettke, T., 2005. Trace element signature of subduction-
280 zone fluids, melts and supercritical liquids at 120-180 km depth. *Nature* 437, 724-727.
- 281 Kumagai, H., Dick, H. J. B., Kaneoka, I., 2003. Noble gas signatures of abyssal gabbros and
282 peridotites at an Indian Ocean core complex. *Geochemistry, Geophysics, Geosystems* 4,
283 9107, doi:10.1029/2003GC000540.
- 284 Kurz, M. D., Jenkins, W. J., Hart, S. R., Clague, D., 1983. Helium Isotopic Variations in
285 Volcanic Rocks from Loihi Seamount and the Island of Hawaii. *Earth and Planetary*
286 *Science Letters* 66, 388-406.
- 287 Kurz, M.D., Jenkins, W. J., 1981. The Distribution of Helium in Oceanic Basalt Glasses. *Earth*
288 and *Planetary Science Letters* 53, 41-54.
- 289 Lawrence, J. F., Shearer, P. M., 2006. A global study of transition zone thickness using receiver
290 functions. *Journal of Geophysical Research* 111, B06307; doi:10.1029/2005JB003973.
- 291 Lee, J. K. W., 1995. Multipath diffusion in geochronology. *Cont. Mineralogy and Petrology*
292 120, 60-82.
- 293 McDonough, W. F., Sun, S.-s., 1995. The composition of the Earth. *Chemical Geology* 120, 223-
294 253.
- 295 Moreira, M., Kurz, M. D., 2001. Subducted oceanic lithosphere and the origin of the 'high μ '
296 basalt helium isotopic signature. *Earth and Planetary Science Letters* 189, 49-57.
- 297 Parman, S. W., Kurz, M. D., Hart, S. R., Grove, T. L., 2005. Helium solubility in olivine and its
298 implications for high $^3He/^4He$ in ocean island basalts. *Nature* 437, 1140-1143.
- 299 Pepin, R.O., Porcelli, D., 2002. Origin of Noble Gases in the Terrestrial Planets, In: Porcelli, D.,
300 Ballentine, C. J., Wieler, R., Eds., Noble gases in geochemistry and cosmochemistry,
301 Reviews in Mineralogy and Geochemistry, Vol. 47, pp. 191-246.
- 302 Roselieb, K., Dersch, O., Büttner, H., Rauch, F., 2006. Diffusivity and solubility of He in
303 garnet: An exploratory study using nuclear reaction analysis. *Nuclear Instruments and*
304 *Methods in Physics Research B: Beam Interactions with Materials and Atoms* 244, 412-
305 418.
- 306 Saal, A. E., Hauri, E. H., Langmuir, C. H., Perfit, M. R., 2002. Vapour undersaturation in

- 307 primitive mid-ocean-ridge basalt and the volatile content of Earth's upper mantle. *Nature*
308 419, 451-455.
- 309 Schmerr, N., Garnero, E., 2006. Investigation of upper mantle discontinuity structure beneath the
310 central Pacific using SS precursors. *Journal of Geophysical Research* 111, B08305,
311 doi:10.1029/2005JB004197.
- 312 Sneeringer, M., Hart, S. R., Shimizu, N., 1984. Strontium and Samarium diffusion in diopside,
313 *Geochim. Cosmochim. Acta*, 48, 1589-1608.
- 314 Staudacher, T., Allègre, C. J., 1988. Recycling of oceanic crust and sediments: the noble gas
315 subduction barrier. *Earth and Planetary Science Letters* 89, 173-183.
- 316 Stixrude, L., Lithgow-Bertelloni, C., 2005a. Mineralogy and elasticity of the oceanic upper
317 mantle: Origin of the low-velocity zone. *Journal of Geophysical Research* 110, (B03204;
318 doi:10.1029/2004JB002965).
- 319 Stixrude, L., Lithgow-Bertelloni, C., 2005b. Thermodynamics of mantle Minerals — I. Physical
320 Properties. *Geophysical J. International* 162, 610-632.
- 321 Trull, T. W., 1989. Diffusion of Helium Isotopes in Silicate Glasses and Minerals: Implications
322 for Petrogenesis and Geochronology. Massachusetts Institute of Technology and Woods
323 Hole Oceanographic Institution.
- 324 Trull, T. W., Kurz, M. D., 1993. Experimental Measurements of ${}^3\text{He}$ and ${}^4\text{He}$ Mobility in Olivine
325 and Clinopyroxene at Magmatic Temperatures. *Geochimica et Cosmochimica Acta* 57,
326 1313-1324.
- 327 Trull, T. W., Kurz, M. D., 1999. Isotopic fractionation accompanying helium diffusion in
328 basaltic glass. *Journal of Molecular Structure* 485-486, 555-567.
- 329 Van Orman, J. A., Fei, Y., Hauri, E. H., Wang, J., 2003. Diffusion in MgO at high pressures:
330 Constraints on deformation mechanisms and chemical transport at the core-mantle
331 boundary. *Geophysical Research Letters* 30, (2), 1056; doi:10.1029/2002GL016343.
- 332 Van Orman, J. A., Grove, T. L., Shimizu, N., 1998. Uranium and thorium diffusion in diopside,
333 *Earth and Planetary Science Letters*, 160, pp. 505-519.
- 334 Van Orman, J. A., Grove, T. L., Shimizu, N., 2001. Rare earth element diffusion in diopside:
335 influence of temperature, pressure and ionic radius, and an elastic model for diffusion in
336 silicates, *Contributions to Mineralogy and Petrology* 141, pp. 687-703.

337
338
339 **Appendix Figure Captions**

- 340
- 341 **Fig. A1.** Arrhenius plot for diffusion of He in various minerals. **Basalt:** MORB tholeiite, 20-
342 600°C, Trull, 1989. **Gnt 1:** grossular-almandine-rich garnet, 800-1300°C, Aciego et al., 2003.
343 **Gnt 3:** pyrope-almandine-rich garnet, 800-990°C, 250 bars, Dunai and Roselieb, 1996. **Gnt 2:**
344 pyrope-almandine-rich garnet, 900-1000°C, 7 kb, Roselieb et al., 2006. **Cpx:** diopside (46:49:5,
345 Wo:En:Fs), 770-1170°C, Trull and Kurz, 1993. **OI 1:** ~ Fo90, 1180-1460°C, Hart, 1984. **OI 2:** Fo

346 89.2, 965-1385°C, Trull and Kurz, 1993. Unless otherwise noted, experiments were conducted in
347 vacuo. The Aciego et al garnet diffusion coefficients were reported as values of D/a^2 ; we used a
348 grain size of 0.86 mm to derive diffusion coefficients in cm^2/s . The relatively low activation
349 energy they determine is not dependent on the choice of grain size (as it was the same at all
350 temperatures). Trull (1989) also determined diffusion coefficients for an alkali basalt glass; these
351 values were consistently lower than the tholeiite by a factor of 3-4. Note that at 1600°C, the
352 diffusion coefficients of elements such as Sr, Nd, Pb, U, Th (in pyroxene) are 3-7 orders of
353 magnitude smaller than the He value of $\sim 1 \times 10^{-6} \text{ cm}^2/\text{s}$ (Sneeringer et al., 1984; Van Orman et
354 al., 1998, 2001; Cherniak, 2001).

355

356 **Fig. A2.** Mean concentration of ${}^4\text{He}$ in semi-infinite slabs of different thicknesses (from 50
357 meters to 10 kilometers), involving both production of ${}^4\text{He}$ from U and Th decay, and diffusion
358 of He into an infinite medium. Present day U content of the slab is taken as 20 ppb, and
359 ${}^{232}\text{Th}/{}^{238}\text{U} = 4.0$ (values for primitive silicate mantle; McDonough and Sun, 1995; Hart and
360 Zindler, 1986). Note that the curves will change concentration linearly with any change in initial
361 U content. The diffusion coefficient of He is taken as $1 \times 10^{-6} \text{ cm}^2/\text{sec}$ (olivine at $\sim 1700^\circ\text{C}$; see
362 Fig. 1). The curve labeled “No diffusion” represents the simple closed-system build-up of ${}^4\text{He}$ by
363 radioactive decay. At the start of the calculation 1.5 Gy ago, the initial U content was 25.2 ppb,
364 with ${}^{238}\text{U}/{}^{235}\text{U} = 39.7$. See text for description of the model formulation (system with zero initial
365 He content, U and Th only inside slab and He content at slab boundary is not fixed, but allowed
366 to float). For verification purposes, the total ${}^4\text{He}$ production in the no-diffusion case today is:
367 $7.7542 \times 10^{-6} \text{ ccSTP/g}$ (STP taken as 0°C and 1 atm).

368

369 **Fig. A3.** Time evolution over 1.5 Gy of (a) ${}^3\text{He}$, (b) ${}^4\text{He}$, (c) ${}^3\text{He}/{}^4\text{He}$ profiles orthogonal to an
370 infinite 1 km slab of ocean crust embedded in an infinite medium of BSE (bulk silicate earth
371 mantle). Model parameters are given in Table 1. Profiles are shown for 1.5 Gy (initial condition),
372 and 1.4, 1.3, 1.0, 0.5 Gy and Today. Panel (d) shows the average ${}^3\text{He}/{}^4\text{He}$ ratios of various size
373 sampling boxes, centered on both a 1 km and a 5 km slab, after either 0.5 Gy or 1.5 Gy of
374 coupled He diffusion and production.

375

376 **Fig. A4.** Nd-He model sampling curves for three model cases: a) - OC slab in DMM matrix; b) -
377 OC slab in BSE matrix; c) - BSE slab in DMM matrix. Sampling curves for various domain
378 widths with diffusion, compared to simple mixing curves without diffusion (after 1.5 Gy, 1 km
379 slab width). The width of sampling domains are shown near selected tic marks on the diffusion
380 curves; the % of slab component is shown near selected tic marks on the no-diffusion mixing
381 curves. In general, the curves with and without diffusion are identical for sampling domains
382 larger than ~ 10 km, but diverge radically for smaller sampling domains. Mixing parameters for
383 He are from Table 1. Sr and Nd for BSE: 19.9 ppm, 0.7050, 1.25 ppm, 0.512638. Sr and Nd for
384 DMM: 7.66 ppm, 0.70263, 0.581 ppm, 0.51313. Sr and Nd for OC: 120 ppm, 0.7040, 7.3 ppm,
385 0.51295.

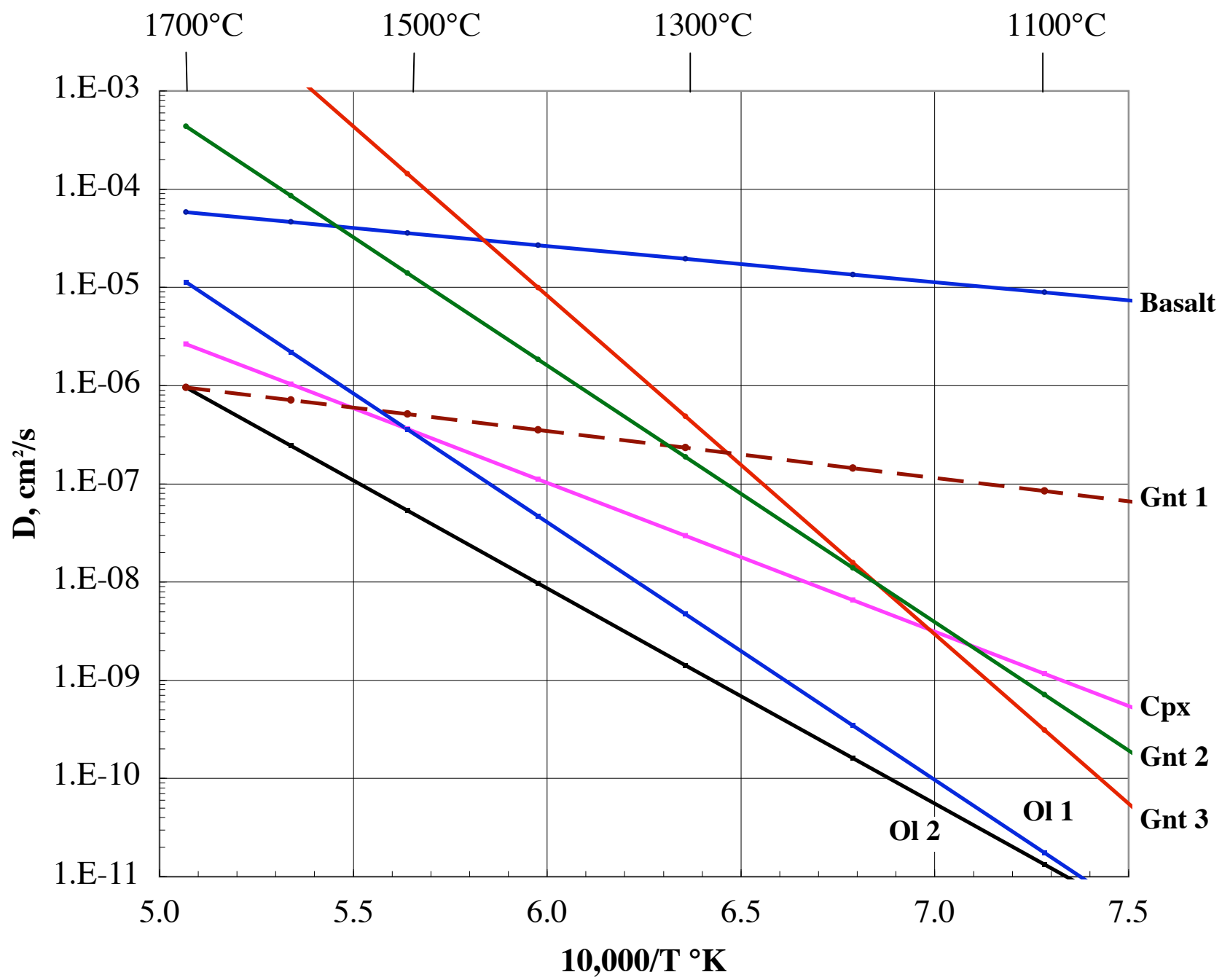


Figure A1

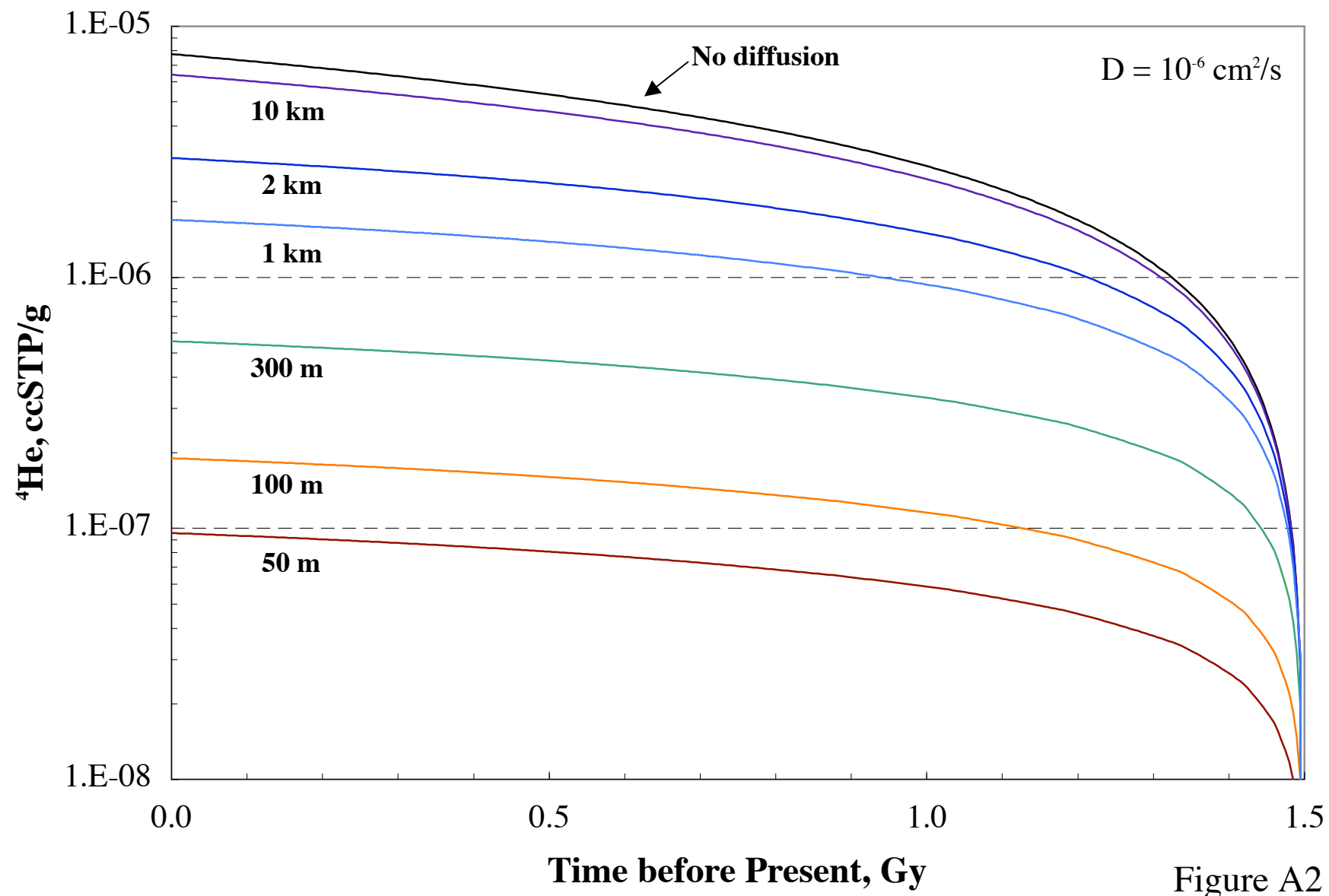


Figure A2

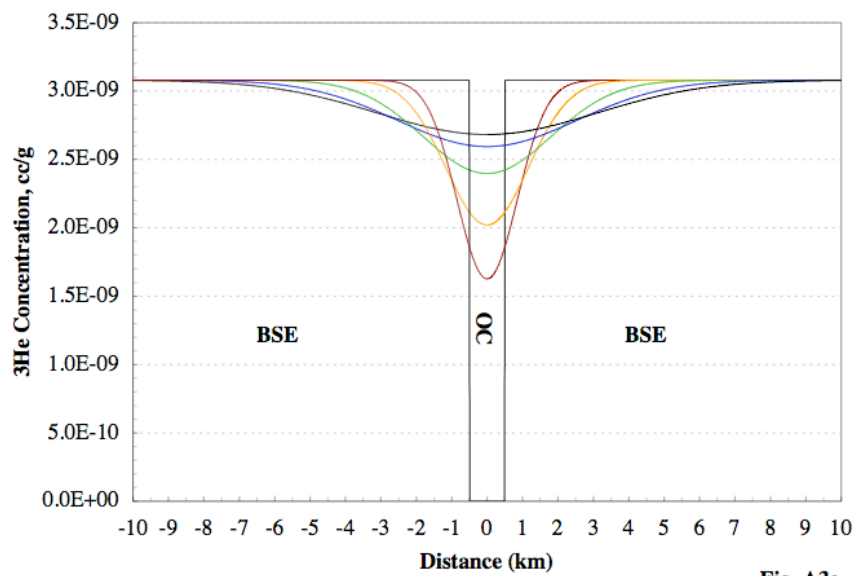


Fig. A3a

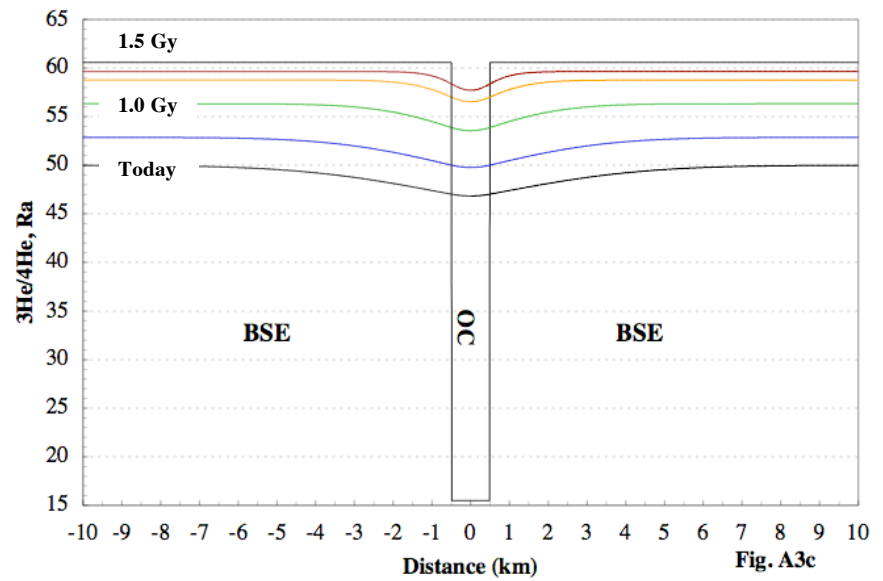


Fig. A3c

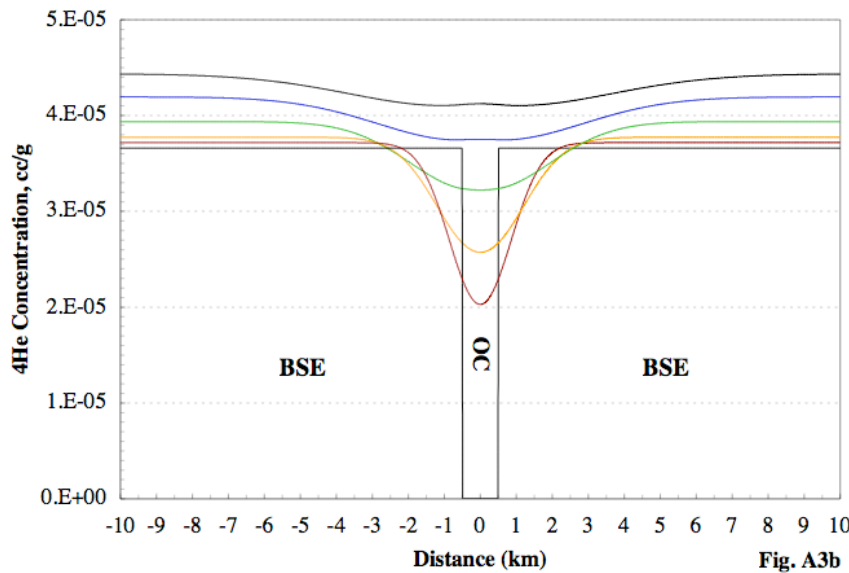


Fig. A3b

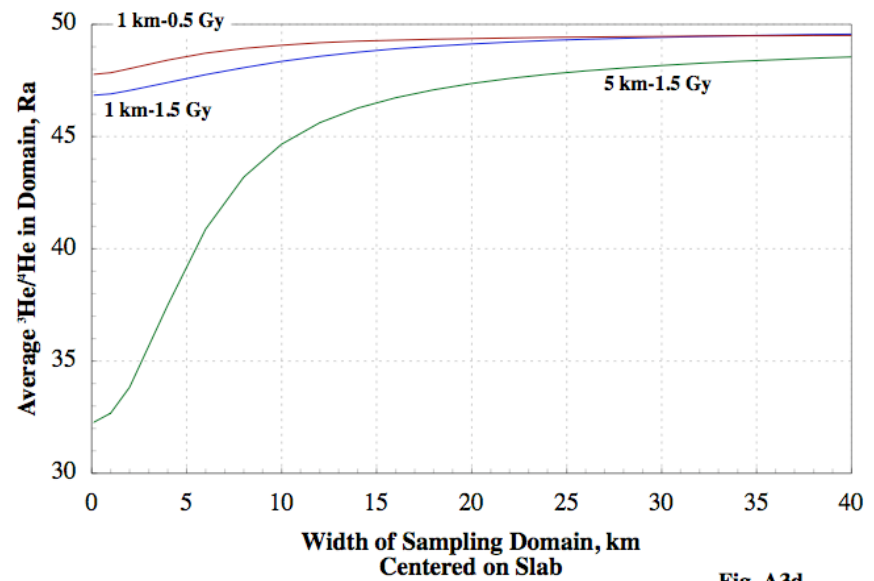
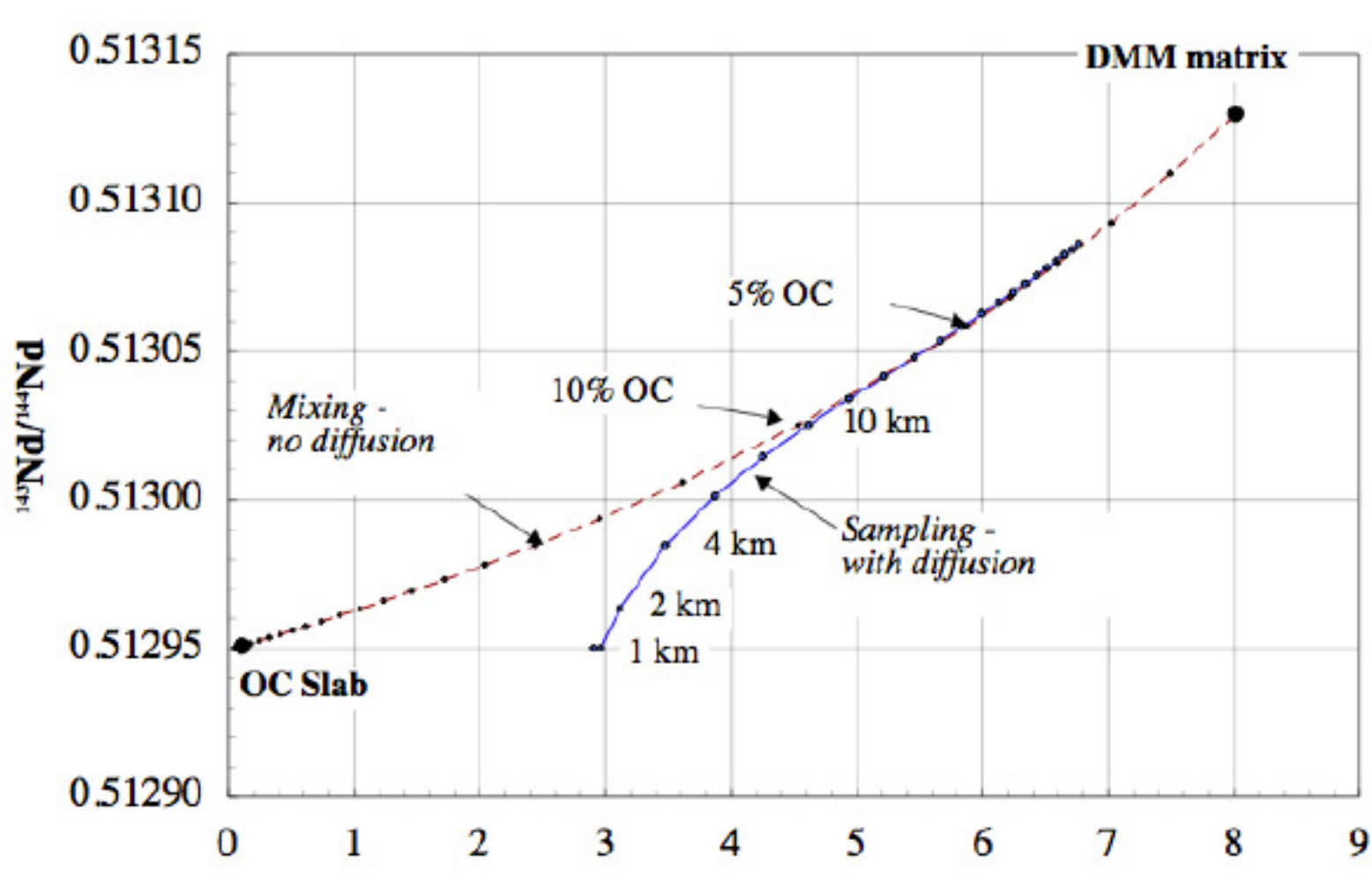
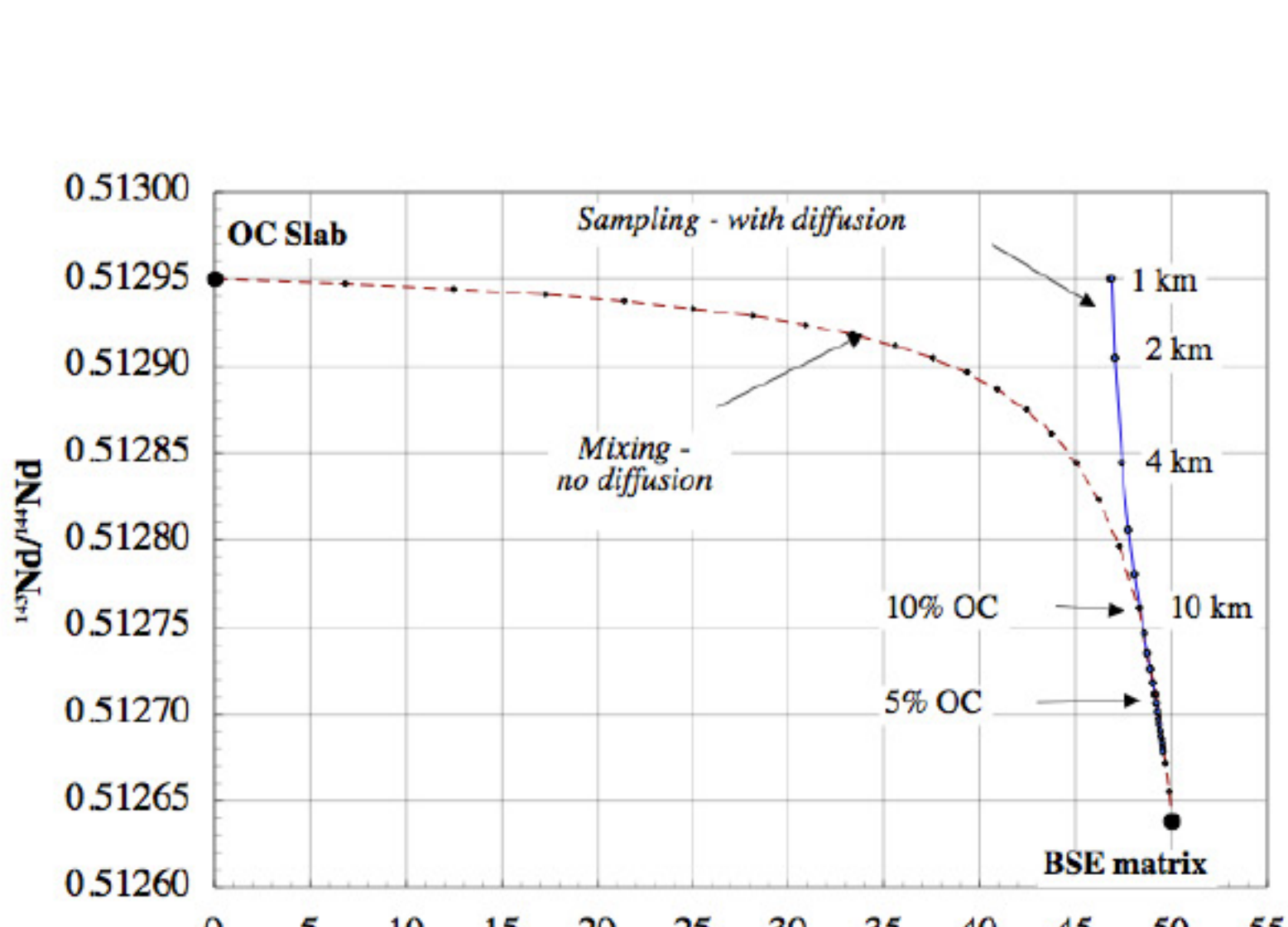


Fig. A3d



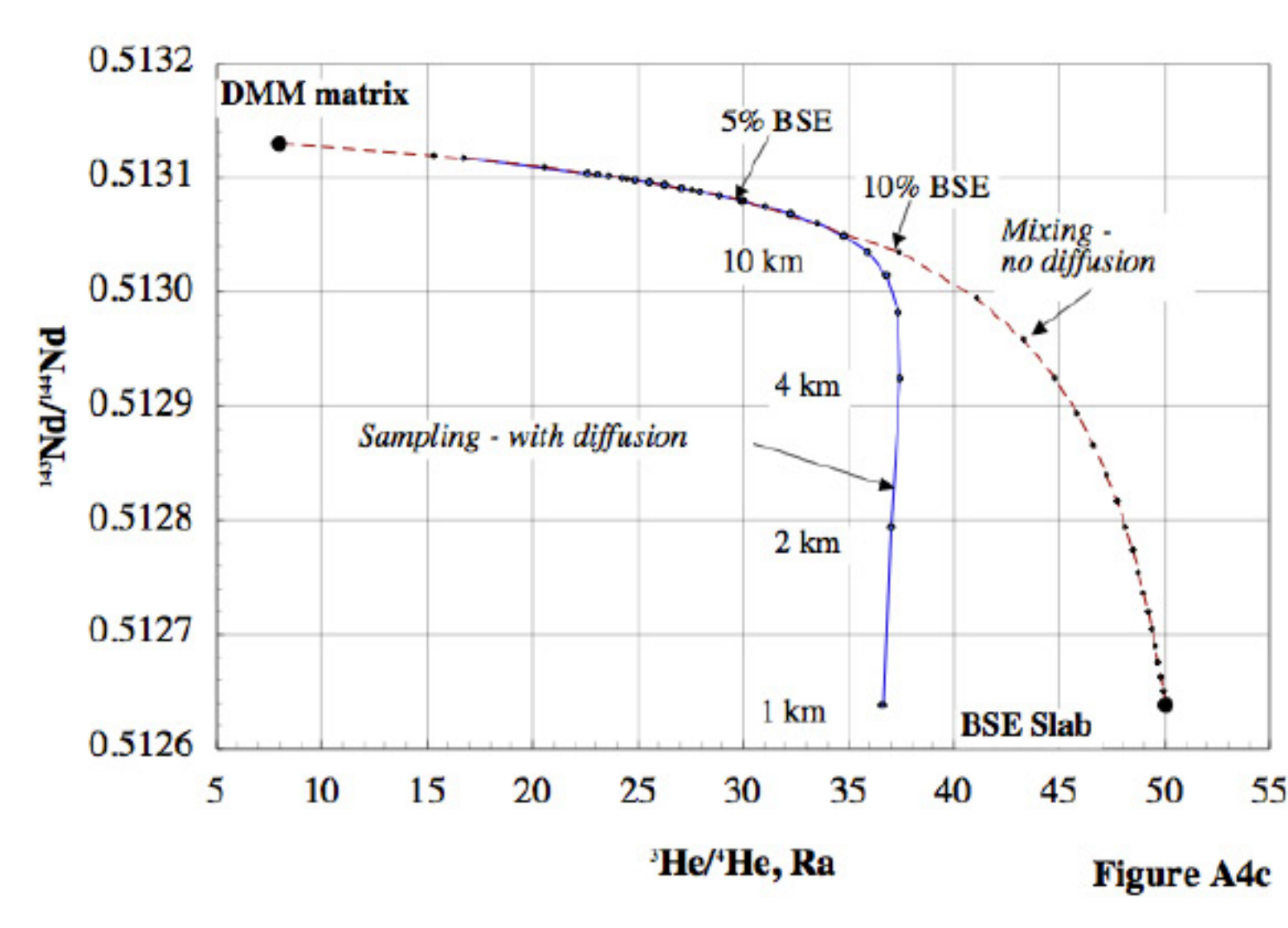
${}^3\text{He}/{}^4\text{He}$, Ra

Figure A4a



${}^3\text{He}/{}^4\text{He}$, Ra

Figure A4b



${}^3\text{He}/{}^4\text{He}$, Ra

Figure A4c